



# Microstructural Characteristics and Mechanical Properties of Cast Mg–3Nd–3Gd–xZn–0.5Zr Alloys

He Xie<sup>1</sup> · Guohua Wu<sup>1</sup> · Xiaolong Zhang<sup>1</sup> · Zhongquan Li<sup>2</sup> · Wencai Liu<sup>1</sup> · Liang Zhang<sup>1</sup> · Xin Tong<sup>1</sup> · Baode Sun<sup>1</sup>

Received: 3 June 2021 / Revised: 8 July 2021 / Accepted: 25 July 2021 / Published online: 29 October 2021  
© The Chinese Society for Metals (CSM) and Springer-Verlag GmbH Germany, part of Springer Nature 2021

## Abstract

The microstructure, aging behavior and mechanical properties of cast Mg–3Nd–3Gd–xZn–0.5Zr ( $x=0, 0.5, 0.8, 1$  wt%) alloys are investigated in this work. Zn–Zr particles with different morphologies form during solution treatment due to the additions of Zn. As the Zn content increases, the number density of Zn–Zr particles also increases. Microstructural comparisons of peak-aged studied alloys indicate that varying Zn additions could profoundly influence the competitive precipitation behavior. In the peak-aged Zn-free alloy,  $\beta''$  phases are the key strengthening precipitates. When 0.5 wt% Zn is added, besides  $\beta''$  precipitates, additional fine  $\beta_1$  precipitates form. With the addition of 0.8 wt% Zn, the peak-aged 0.8Zn alloy is characterized by predominantly prismatic  $\beta_1$  and scanty basal precipitate distributions. The enhanced precipitation of  $\beta_1$  should be primarily attributable to the presence of increased Zn–Zr dispersoids. When Zn content further increases to 1 wt%, the precipitation of basal precipitates is markedly enhanced. Basal precipitates and  $\beta_1$  phases are the key strengthening precipitates in the peak-aged 1Zn alloy. Tensile tests reveal that the relatively best tensile properties are achieved in the peak-aged alloy with 0.5 wt% Zn addition, whose yield strength, ultimate tensile strength and elongation are 179 MPa, 301 MPa and 5.3%, respectively.

**Keywords** Mg–Nd–Gd alloy · Zn addition · Competitive precipitation behavior · Microstructural characterization

## 1 Introduction

Cast magnesium alloys containing rare-earth (RE) elements have received considerable attention because of their low density and high specific strength [1–3]. In the past, extensive works have been published on Mg–Gd and Mg–Nd system alloys due to their enhanced mechanical properties [4, 5]. High-performance cast Mg–Gd alloys often contain a high concentration of element Gd (10–20 wt%) to efficiently

improve the age-hardening response [6]. However, the high total RE content significantly increases the cost and limits the practical applications of Mg–Gd alloys. Recently, there has been renewed interest in developing high-strength Mg–Nd alloys since they have great capabilities in providing significant precipitation-hardening responses with relatively lower RE contents ( $\leq 6$  wt%) [7–9]. For instance, Mg–3Nd–0.2Zn (wt%) alloy, designated as NZ30K, is one of the successfully developed cast Mg–Nd alloys with high strength, good ductility and high creep resistance [10, 11]. Recently, there are several investigations carried out to further improve the mechanical properties of Mg–Nd alloys [10, 12]. Our previous work reveals that additions of Gd can efficiently enhance the age-hardening response of cast Mg–Nd alloys [12]. It is of interest to develop novel high-performance Mg–Nd–Gd-based alloys with relatively low RE contents ( $\leq 6$  wt%).

Zn is an alloying element widely used in Mg–RE alloys [13, 14]. Additions of Zn can significantly enhance the precipitation-hardening response of Mg–Gd alloys, which is primarily due to the formation of dense strengthening precipitates lying on  $(0001)_\alpha$  planes of the Mg matrix [15, 16].

Available online at <http://link.springer.com/journal/40195>.

- ✉ Guohua Wu  
ghwu@sjtu.edu.cn
- ✉ Xiaolong Zhang  
XLZhang1993@sjtu.edu.cn

<sup>1</sup> National Engineering Research Center of Light Alloy Net Forming and State Key Laboratory of Metal Matrix Composites, School of Materials Science and Engineering, Shanghai Jiao Tong University, Shanghai 200240, China

<sup>2</sup> Shanghai Spaceflight Precision Machinery Institute, Shanghai 201600, China

Moreover, additions of Zn have been reported to efficiently enhance the strength and creep resistance of Mg–Y alloys by introducing long period stacking ordered (LPSO) structures [17–20]. For Mg–Nd alloy, a recent study indicates that the mechanical properties of cast Mg–1Nd–1Ce–Zn alloy can be effectively improved by the optimized addition of Zn [21]. The role of Zn on the microstructure and mechanical properties of cast Mg–Nd–Gd-based alloys is not clear yet.

The purpose of the present work is to investigate the influence of different Zn additions (0, 0.5, 0.8, 1 wt%) on the microstructure, aging behavior and mechanical properties of cast Mg–3Nd–3Gd–0.5Zr alloy. Precipitate microstructures of Mg–3Nd–3Gd–xZn–0.5Zr alloys peak-aged at 200 °C are characterized and compared. The alterations in mechanical properties of studied alloys are discussed and rationalized according to the microstructural characterization.

## 2 Experimental

Cast Mg–3Nd–3Gd–xZn–0.5Zr ( $x=0, 0.5, 0.8, 1$  wt%) alloys were prepared by melting high purity Mg (99.99 wt%), high purity Zn (99.99 wt%), and master alloys of Mg–30Gd (wt%), Mg–30Nd (wt%) and Mg–30Zr (wt%) in a mild steel crucible at approximately 750 °C under a mixing atmosphere of CO<sub>2</sub> and SF<sub>6</sub>. They were hereafter designated as the base, 0.5Zn, 0.8Zn and 1Zn alloys for brevity, respectively. The actual chemical compositions were determined using inductively couple plasma-atomic emission spectroscopy (ICP-AES), and the results are listed in Table 1.

Cast ingots were solution-treated at 525 °C for 8 h and immediately water quenched to room temperature. As-quenched samples were isothermally aged at 200 °C for various times up to 1024 h. During the aging treatment, hardnesses of the alloys were measured with a load of 50 N and a maintaining time of 15 s (each value was obtained by taking the average of at least seven individual measurements). A Zwick/Roell Z020 testing machine was used to conduct the tensile tests with a constant strain rate of  $5 \times 10^{-4}$  s<sup>-1</sup>. Specimens for tensile tests were cut into dog-bone shapes with the width of 3.5 mm, the thickness of 2 mm and the gauge length of 10 mm, respectively.

**Table 1** Actual chemical compositions of cast Mg–3Nd–3Gd–xZn–0.5Zr ( $x=0, 0.5, 0.8, 1.0$  wt%) alloys

Alloys	Actual compositions			
	Nd (wt%)	Gd (wt%)	Zn (wt%)	Zr (wt%)
Base	3.05	3.08	–	0.43
0.5Zn	3.01	3.04	0.48	0.42
0.8Zn	2.99	3.06	0.79	0.42
1Zn	3.08	3.10	1.05	0.46

X-ray diffractometer (XRD, Rigaku Ultima IV) was used to determine the phases in as-cast alloys. All metallographic samples were mechanically grounded and polished, then etched by a reagent consisting of 10 ml H<sub>2</sub>O, 5 ml acetic acid, 5 g picric acid, and 100 ml ethanol and observed by the optical microscopy (OM, Zeiss Axio observer) and scanning electron microscopy (SEM, Zeiss ULTRA55). Precipitate characterization was performed in a transmission electron microscope (TEM, a JEOL-2100F and an FEI Talos F200X). TEM thin foils were prepared by twin jet electropolished in a solution (4% HClO<sub>4</sub> and 96% C<sub>2</sub>H<sub>5</sub>OH) cooled from –20 to –25 °C using a potential of 20 V.

## 3 Results

### 3.1 As-Cast Microstructure

Figure 1 shows typical microstructures of as-cast Mg–3Nd–3Gd–xZn–0.5Zr alloys. As-cast alloys are composed of  $\alpha$ -Mg matrix and secondary phases distributed along grain boundaries. The volume fraction of secondary phases increases with increasing addition of Zn, while no appreciable grain refinement is revealed. The measured average grain sizes of as-cast Mg–3Nd–3Gd–xZn–0.5Zr alloys are 22  $\mu$ m, 26  $\mu$ m, 26  $\mu$ m and 24  $\mu$ m, respectively.

Figure 2 exhibits representative SEM micrographs showing the morphology of secondary phases in as-cast alloys. It is observed that the secondary phases present a bone-like shape and gradually distribute in a continuous network with increasing Zn addition. Chemical compositions of secondary phases, determined by EDS point analysis (positions marked by arrows in Fig. 2a–d), are listed in Table 2. It is noticeable that, with the increased addition of Zn, the atomic fraction of Zn in the secondary phases increases, accompanied by simultaneous enhancements of the total content of rare-earth elements. Based on the XRD patterns presented in Fig. 3, the as-cast base alloy mainly consists of  $\alpha$ -Mg and secondary Mg<sub>5</sub>(Gd, Nd) phases. It is noticeable that, with the addition of Zn, the characteristic diffraction peaks related to Mg<sub>5</sub>(Gd, Nd) phases disappear. Besides, some extra diffraction peaks are revealed, which are found to be coincident with the characteristic diffraction peaks related to (Mg, Zn)<sub>3</sub>(Gd, Nd) phase. The relative intensity of diffraction peaks associated with (Mg, Zn)<sub>3</sub>(Gd, Nd) is gradually improved as the increase in Zn addition (illustrated in Fig. 3). It can be inferred that the (Mg, Zn)<sub>3</sub>(Gd, Nd) phase should be the predominantly secondary phase in as-cast Zn-containing studied alloys.

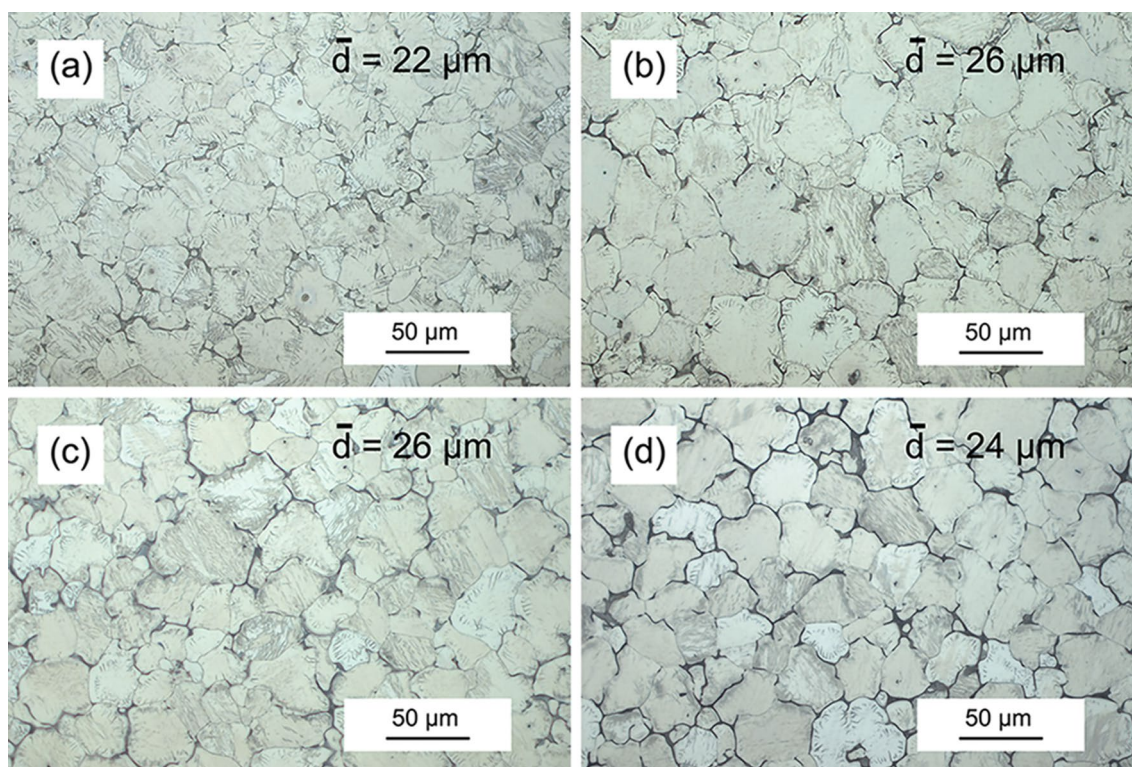


Fig. 1 Optical microstructure of as-cast alloys: **a** base alloy, **b** 0.5Zn alloy, **c** 0.8Zn alloy, **d** 1Zn alloy

### 3.2 As-Quenched Microstructure

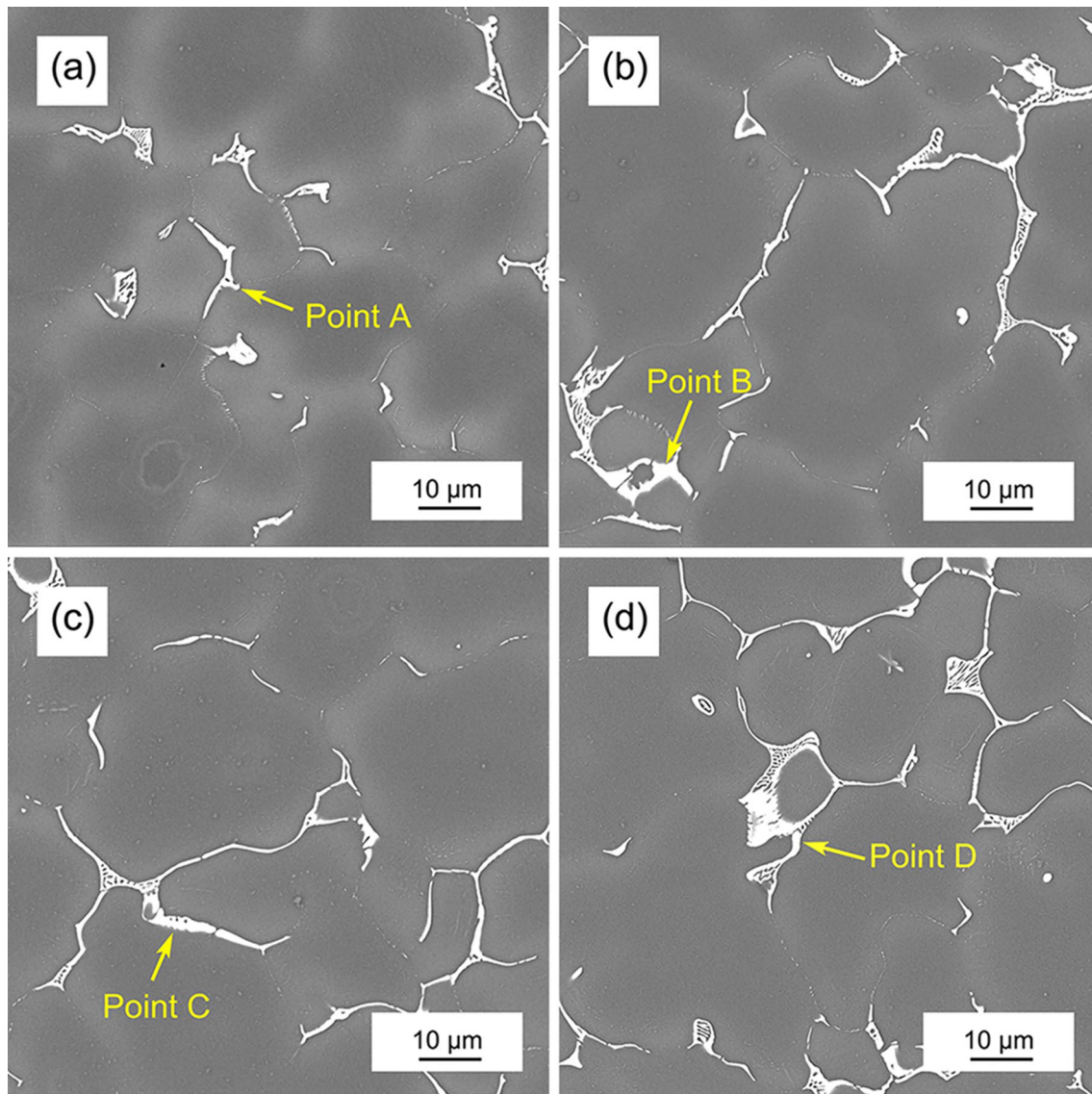
Figure 4 presents OM images of as-quenched alloys. After subjected to the solution treatment, for the base and 0.5Zn alloys (Fig. 4a, b), most of the secondary phases distributed along the grain boundaries are dissolved into the matrix. Meanwhile, some dark spots appear in the as-quenched base alloy, while rosette-like patches are visible within the grains in the as-quenched 0.5Zn alloy. For the 0.8Zn and 1Zn alloys, as illustrated in Fig. 4c, d, besides the increased rosette-like patches, sparse distribution of residual second phases is also detected at the triple points of grain boundaries.

Figure 5 shows SEM images illustrating the spots and the rosette-like patches observed in Fig. 4. As shown in Fig. 5a, the spots observed in the as-quenched base alloy (illustrated in Fig. 4a) are noticed to be cuboid-shaped phases with sizes of about 1–3  $\mu\text{m}$ . The corresponding EDS point analysis results in Fig. 6 show that these cuboid-shaped phases are abundant in Gd and Nd, similar to these reported cuboid-shaped RE-rich phases with an fcc structure [22]. As illustrated in Fig. 5b–d, uneven distributions of numerous particles within the grains of Zn-containing alloys are observed. The distribution patches of these particles take a rosette morphology, which is noticeably similar to that observed in Fig. 4b–d. High-angle annular dark-field scanning

transmission electron microscopy (HAADF-STEM) images of the as-quenched 1Zn alloy (provided in Fig. 7a, b) illustrate that most of these particles within the grains show a rod-like morphology, while a small part of them is globular. Meanwhile, the corresponding EDS elemental maps illustrated in Fig. 7c–f show that Zn and Zr are strongly enriched in these particles. Therefore, they are considered the reported Zn–Zr particles in as-quenched Mg–RE–Zn–Zr alloys, which have been identified as  $\text{Zn}_2\text{Zr}_3$  phases [23].

### 3.3 Age-Hardening Responses

Age-hardening curves of four studied alloys isothermally aged at 200  $^\circ\text{C}$  are compared in Fig. 8. It is to be noted that the as-quenched base alloy possesses a hardness of 53 HV. Upon the aging treatment, the hardness of the base alloy increases sharply, reaching a peak of 85 HV at 16 h and then gradually decreases with the prolonged aging time. The hardness (56 HV) of the as-quenched 0.5Zn alloy is slightly higher than that of the base alloy. Firstly, the hardness of the 0.5Zn alloy also increases quickly and achieves a peak of 91 HV at 16 h, which is 6 HV higher than that of the base alloy. Then, the hardness of the 0.5Zn alloy decreases as the aging time increases. The 0.8Zn alloy exhibits a hardness of 59 HV in the as-quenched condition. At the early stage of aging, the age-hardening



**Fig. 2** SEM micrographs showing the morphology of secondary phases: **a** base alloy, **b** 0.5Zn alloy, **c** 0.8Zn alloy, **d** 1Zn alloy. The positions for EDS point analysis are indicated by arrows

**Table 2** EDS point analysis results of the secondary phases in as-cast alloys

Alloy	Point	Atomic percentage (at.%)				
		Mg	Nd	Gd	Zn	Zr
Base	A	92.80	6.14	1.06	0.00	0.00
0.5Zn	B	81.95	5.85	2.92	9.28	0.00
0.8Zn	C	74.80	8.20	3.20	13.80	0.00
1Zn	D	71.86	8.18	2.43	17.53	0.00

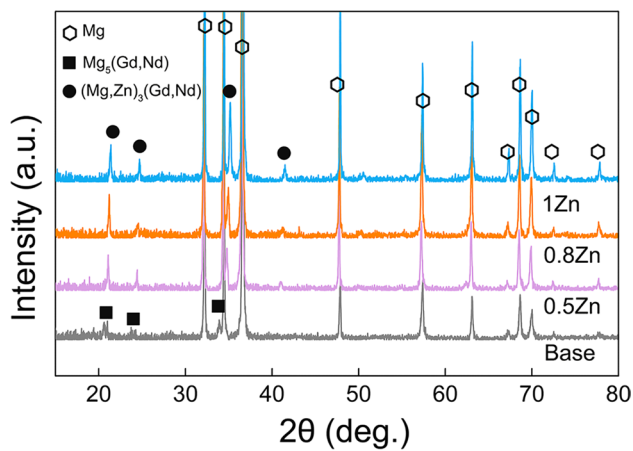


Fig. 3 XRD patterns of as-cast Mg-3Nd-3Gd-xZn-0.5Zr alloys

response of the 0.8Zn alloy is slower than that of the base and 0.5Zn alloy. After aging for 2 h, the hardness of the 0.8Zn alloy increases quickly. The peak hardness (87 HV) of the 0.8Zn alloy is achieved after 16 h. The as-quenched 1Zn alloy shows a hardness of 60 HV, close to that of the 0.8Zn alloy. Within the first 2 h of aging treatment, the age-hardening response of the 1Zn alloy is slower than that of the 0.8Zn alloy. In the following aging time, the

hardness of the 1Zn alloy increases rapidly and reaches the highest hardness (86 HV) at 16 h. According to these age-hardening curves, it is inferred that trace 0.5 wt% addition of Zn leads to the enhanced precipitation hardening of the base alloy. However, precipitation hardening in the 0.8Zn and 1Zn alloys will be weakened when Zn content exceeds 0.8 wt%.

### 3.4 Peak-Aged Microstructure

The precipitate microstructures of peak-aged alloys are carefully characterized to clarify the different age-hardening responses associated with various Zn additions.

#### 3.4.1 Peak-Aged Base Alloy

Figure 9a, b shows bright-field (BF) images taken from the base alloy peak-aged at 200 °C with the incident beam parallel to  $[0001]_{\alpha}$  direction, which are characterized by numerous fine lenticular precipitates. It is observed that most of these precipitates are lying on  $\{11\bar{2}0\}_{\alpha}$  matrix planes with an aspect ratio of over 10:1. The corresponding selected area electron diffraction (SAED) patterns (inset in Fig. 9a, c) reveal the presence of extra characteristic reflections at  $1/2 <01\ 1\ 0>_{\alpha}$  positions. These precipitates can be inferred

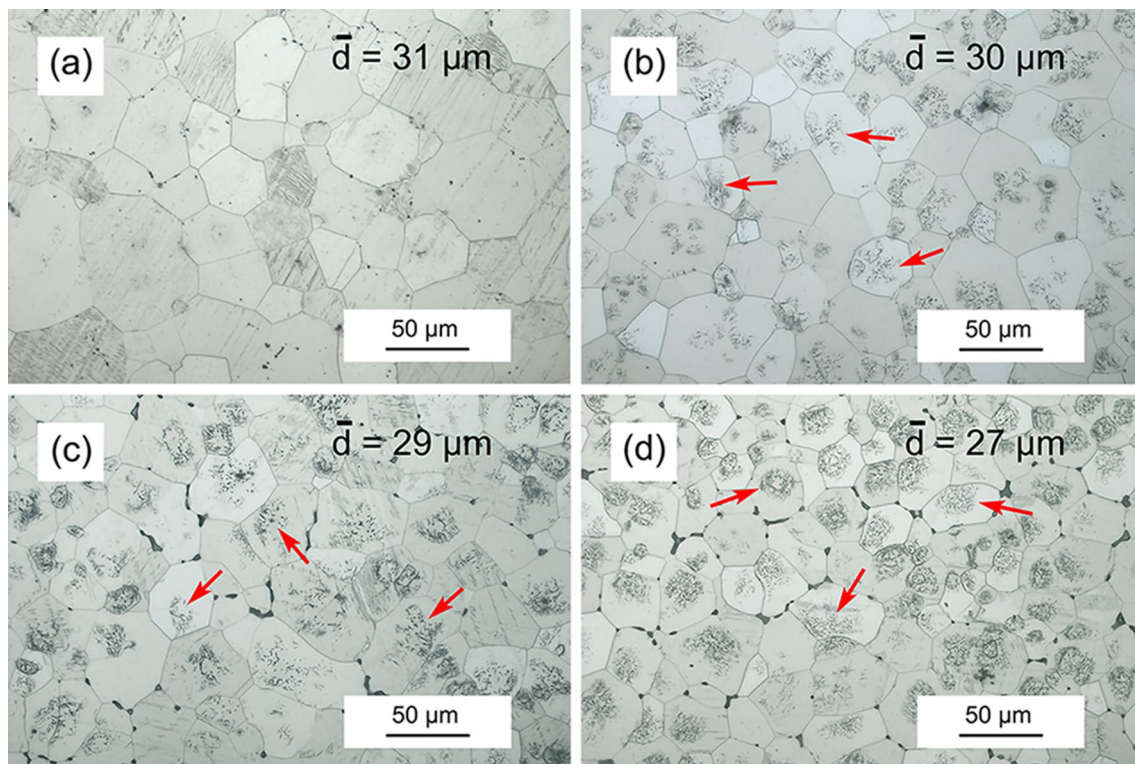
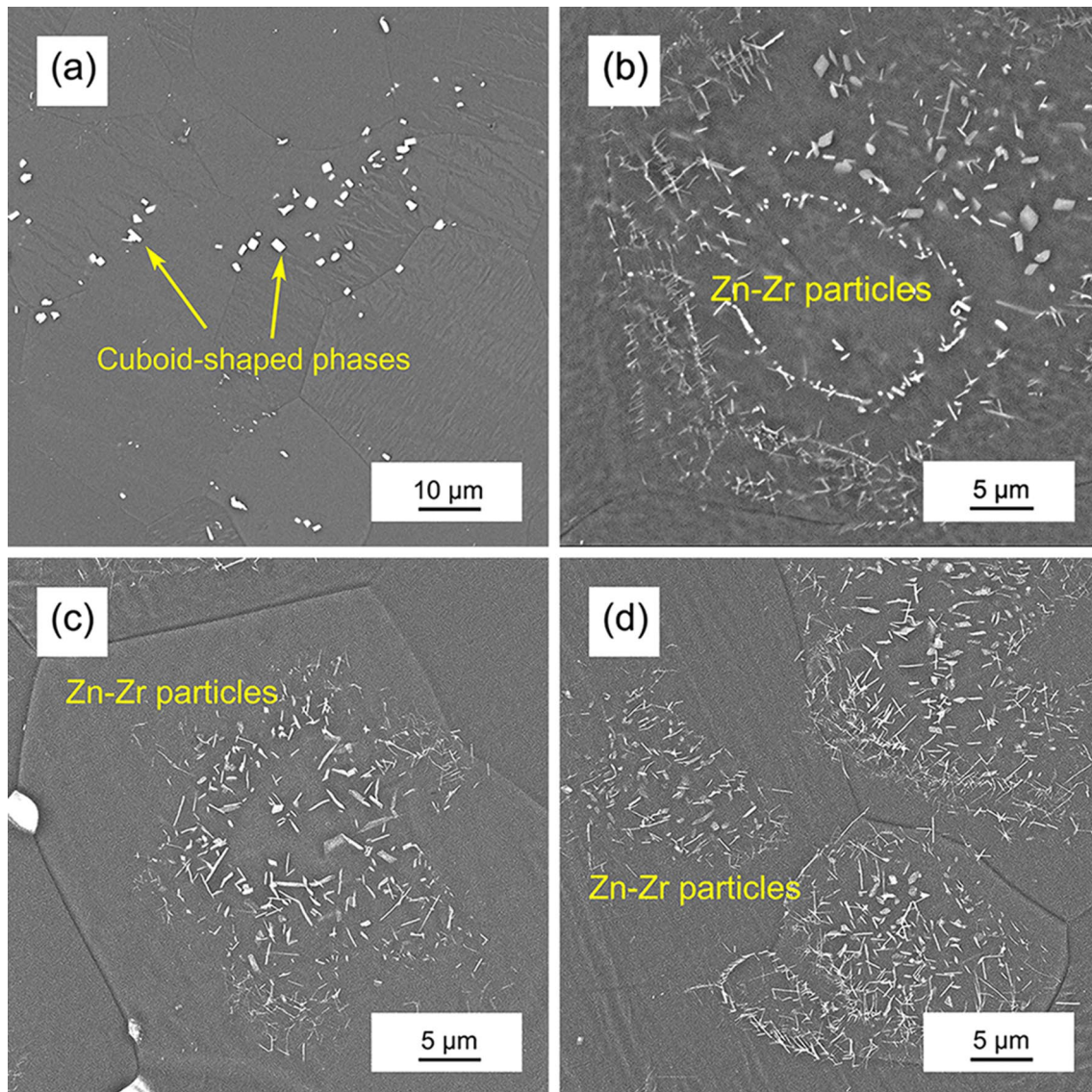


Fig. 4 Microstructure of as-quenched alloys: **a** base alloy, **b** 0.5Zn alloy, **c** 0.8Zn alloy, **d** 1Zn alloy. Note that patches with rosette-like shapes appear in the Zn-containing alloys (marked by the arrows)



**Fig. 5** Backscattered SEM micrographs illustrating the presence of cuboid-shaped phases and Zn–Zr particles in as-quenched alloys: **a** base alloy, **b** 0.5Zn alloy, **c** 0.8Zn alloy, **d** 1Zn alloy

to be  $\beta''$  phases with  $D0_{19}$  structure, and the orientation relationship between the  $\beta''$  and the  $\alpha$ -Mg matrix is reported as:  $[0001]_{\beta''} // [0001]_{\alpha}$  and  $(01\bar{1}0)_{\beta''} // (0110)_{\alpha}$  [24]. As can be seen in Fig. 9c, d, the  $[2110]_{\alpha}$  BF images also show the dispersion of prismatic  $\beta''$  phases.

### 3.4.2 Peak-Aged 0.5Zn Alloy

As shown in Fig. 10a, b, dense distribution of fine matrix precipitates is also observed in the peak-aged 0.5Zn alloy. The corresponding SAED pattern inset in Fig. 10a reveals no additional reflections besides  $\alpha$ -Mg matrix. In Fig. 10b, as shown by yellow arrows, these thin  $\{11\bar{2}0\}_{\alpha}$  precipitates are  $\beta''$  phases, which are consistent with those observed in the

base alloy. Besides, the precipitates indicated by red arrows exhibit a different morphology compared to that of  $\beta''$ . The structure of these peculiar precipitate interactions will be detailed in the following. As can be seen in Fig. 10c, d, BF micrographs taken along  $[2110]_{\alpha}$  direction also reveal the presence of prismatic precipitates.

Figure 11 provides typical  $[0001]_{\alpha}$  HAADF-STEM images illustrating the peculiar precipitate interactions in Fig. 10b. Because the atomic number of RE (Nd/Gd) atoms is greater than that of Mg, the contrast of RE atoms will be brighter when observed in HAADF-STEM micrographs [25, 26]. Therefore, the bright dots observed in Fig. 11 are supposed to be RE-rich columns. As illustrated by the corresponding magnified regions in Fig. 11, two different and

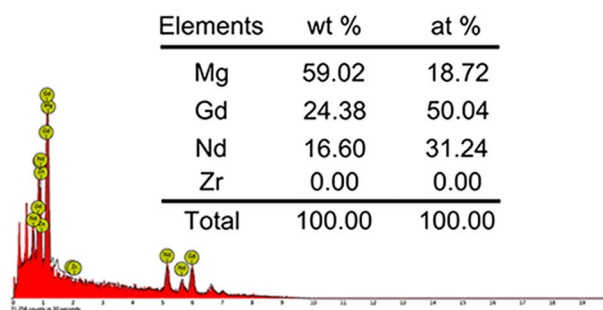
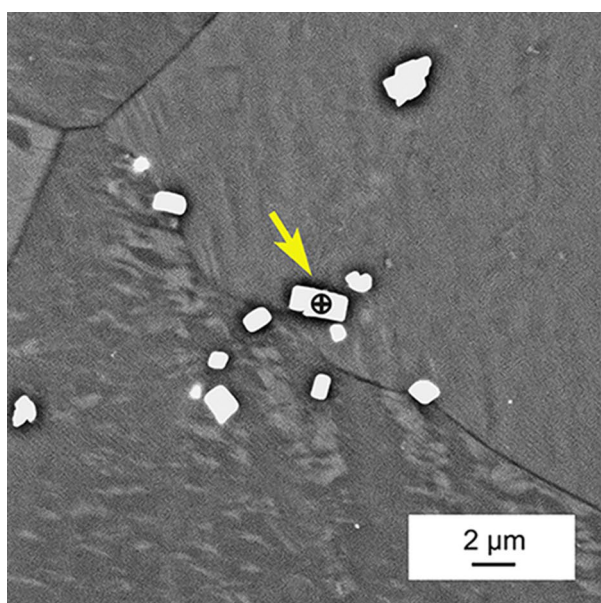


**Fig. 6** EDS point analysis of cuboid-shaped phases noticed in the as-quenched base alloy

typical characteristics are observed. The one is hexagons (noted by the arrow in Fig. 11a), which is a specific characteristic of  $\beta''$  with a  $D0_{19}$  structure according to the previous studies [12, 25]. Moreover, the corresponding magnified region in Fig. 11b reveals a different centered rectangular lattice noted by the arrow, consistent with the typical arrangement of atomic columns along a  $\langle 110 \rangle$  direction of  $\beta_1$  phases with an fcc structure [25, 26]. It is indicated that some fine  $\beta_1$  phases form in association with  $\beta''$  phases and they are likely to be in contact with the hexagonal arrays of  $\beta''$  phases.

### 3.4.3 Peak-Aged 0.8Zn Alloy

Figure 12a, b provides representative TEM micrographs taken from the peak-aged 0.8Zn alloy observed along  $[0001]_\alpha$

direction. Dense distribution of coarser plate-shaped precipitates lying on  $\{10\ 1\ 0\}_\alpha$  planes is observed. According to their typical crystallographic orientations and dimensions, these  $\{10\ 1\ 0\}_\alpha$  precipitates are supposed to be prismatic  $\beta_1$  with an fcc structure [24]. In addition to prismatic  $\beta_1$  phases, BF micrographs obtained with the electron beam parallel to  $[2\ 11\ 0]_\alpha$  (shown in Fig. 12c, d) also reveal the existence of sparsely dispersed basal plates on  $(0001)_\alpha$  matrix planes. Note that these basal plates are approximately 1 nm thick and have a significantly large aspect ratio (above 200:1), which is similar to those  $\gamma'$  precipitates reported in Mg–RE–Zn alloys [24].

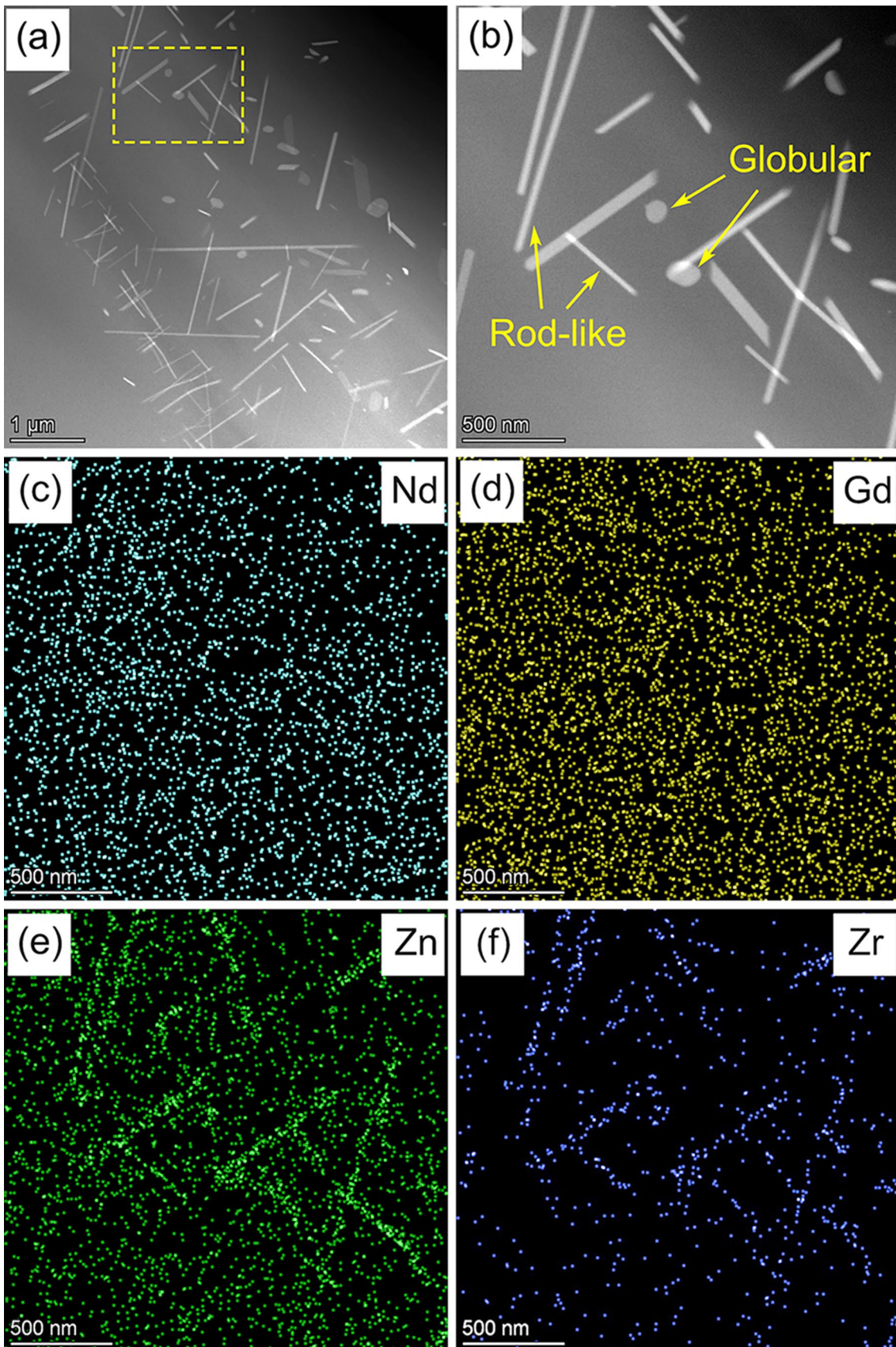
### 3.4.4 Peak-Aged 1Zn Alloy

Figure 13a, b shows the microstructure of the peak-aged 1Zn alloy, observed in the  $[0001]_\alpha$  direction, illustrating the existence of plate-shaped  $\beta_1$  phases lying on  $\{10\ 1\ 0\}_\alpha$  planes. Additionally, TEM images taken along  $[2\ 11\ 0]_\alpha$  zone axis indicate that the peak-aged 1Zn alloy also involves the formation of basal  $(0001)_\alpha$  plates as evidenced by Fig. 13c, d. In the peak-aged 1Zn alloy, it is noticeable that the number density of basal precipitates is significantly enhanced when compared with the peak-aged 0.8Zn alloy, which is in agreement with the appearance of extra sets of reflections at  $1/3\ \{11\ 2\ 0\}_\alpha$  positions observed in the SAED pattern (inserted in Fig. 13a). It is also noted that these basal plates have a similar thickness (about 1 nm) but significantly smaller aspect ratios ( $<40:1$ ) compared with that in the peak-aged 0.8Zn alloy. Thus, the majority of basal plates in the peak-aged 1Zn alloy are  $\gamma''$  [24, 27].

## 3.5 Mechanical Properties

Figure 14 illustrates engineering strain–stress curves and corresponding ambient tensile properties, involving ultimate tensile strength (UTS), yield strength (YS) and elongation (EL) of Mg–3Nd–3Gd– $x$ Zn–0.5Zr alloys under different conditions. For as-cast studied alloys, as illustrated in Fig. 14a, b, the UTS and EL are gradually decreased with increasing addition of Zn. No appreciable difference in YS is revealed in the as-cast Zn-containing alloy, which are slightly lower than that of the as-cast base alloy.

Figure 14c, d provides mechanical properties of as-quenched Mg–3Nd–3Gd– $x$ Zn–0.5Zr alloys. With the increase in Zn addition, the UTS and EL of as-quenched alloys are





**Fig. 7** **a** HAADF-STEM image showing Zn–Zr particles with different morphologies in the as-quenched 1Zn alloy; **b** enlarged image corresponding to the region marked by the dotted frame in **a**; elements map-scanning of **c** Nd; **d** Gd; **e** Zn, **f** Zr

successively increased compared with those of the base alloy. The as-quenched 1Zn alloy possesses the relatively best combination of strength and ductility (UTS = 192 MPa, YS = 109 MPa and EL = 12.5%).

For the studied alloys in peak-aged condition, as evidenced by Fig. 14e, f, both YS and UTS increase firstly and then decrease with increasing Zn addition. The highest YS and UTS are achieved in the 0.5Zn alloy, respectively, 179 MPa and 301 MPa. In contrast, the EL of the studied alloys decreases firstly and then increases as the Zn content increases from 0 to 1 wt%.

## 4 Discussion

### 4.1 Heterogeneous Nucleation of $\beta_1$ Associated with Zn–Zr Particles

Figure 15a shows a specific HAADF-STEM micrograph taken from the peak-aged 1Zn alloy illustrating the unique interaction between  $\beta_1$  phase and a spherical particle. The corresponding EDS chemical maps are provided in Fig. 15b–f. Related EDS elemental maps presented in Fig. 15b through f reveal that Nd, Gd and Zn are strongly enriched in  $\beta_1$ . Besides, significant enrichments of Zn and Zr in the spherical particle are discerned. Accordingly, the spherical particle is supposed to be a Zn–Zr particle noticed in as-quenched alloys (shown in Fig. 7). Figure 16 also confirms the specific interaction between the rod-like Zn–Zr particles and  $\beta_1$  precipitates, indicating that Zn–Zr particles perform as the preferential sites for the heterogeneous nucleation of  $\beta_1$ .

Zn–Zr particles are reported to be  $Zn_2Zr_3$  phases with a tetragonal structure ( $a = b = 7.633$  nm,  $c = 6.965$  nm,  $\alpha = \beta = \gamma = 90^\circ$ ) [23, 28]. Due to the significant difference between the crystal structure of the Mg matrix (hcp structure,  $a = 0.321$  nm,  $c = 0.521$  nm) and  $Zn_2Zr_3$ , the formation of these  $Zn_2Zr_3$  particles in the magnesium matrix will inevitably result in the formation of structural factors, such as defects and strains, in the adjacent area of the interfaces between  $Zn_2Zr_3$  phases and Mg matrix. These structural factors are likely to provide a lower activation energy barrier for the nucleation of the subsequent  $\beta_1$  precipitates based on classical nucleation theory [29]. In addition, it is also reported previously that the inter-planar misfit value between the matching planes of  $Zn_2Zr_3$  and  $\beta_1$  is lower than the critical value provided by the edge-to-edge model [30], indicating that the existence of the Zn–Zr particles can provide a

favorable crystallographic correlation for the nucleation of the subsequent  $\beta_1$  precipitates. Overall, due to the existence of Zn–Zr particles, the lower activation energy barrier and favorable crystallographic correlation for the nucleation of  $\beta_1$  precipitates facilitate the heterogeneous nucleation of  $\beta_1$ .

### 4.2 Competitive Precipitation Behavior Associated with Varying Zn Additions

As illustrated in Table 3, Zn content significantly influences the precipitate microstructure of peak-aged alloys. In the peak-aged base alloy, the matrix precipitation is composed of dense fine  $\beta''$  precipitates. When 0.5 wt% Zn is added, besides  $\beta''$  precipitates, fine prismatic  $\beta_1$  phases form in the matrix. With the addition of 0.8 wt% Zn, there are almost no  $\beta''$  precipitates, and  $\beta_1$  phases are the key strengthening precipitates, accompanied by a scanty distribution of basal precipitates. As Zn addition further increases to 1 wt%, the number density of basal precipitates significantly increases. The matrix precipitation of the peak-aged 1Zn alloy is characterized by the coexistence of prismatic  $\beta_1$  precipitates and dense basal precipitates.

The enhanced precipitation of  $\beta_1$  observed in the Zn-containing alloys could be mainly attributed to two aspects. On the one hand, as shown in Figs. 15 and 16, since Zn is obviously enriched in  $\beta_1$  phases. It can be inferred that Zn participates in the formation of  $\beta_1$  precipitate, thereby promoting the precipitation of  $\beta_1$ . On the other hand, as previously reported, the shear strain energy produced by the nucleation of  $\beta_1$  (considered as the resistance to nucleation) could be efficiently eliminated by the extrinsic supply of corresponding existing concentrations of vacancies [31]. Those alloying elements possessing high binding energies with vacancies might be capable of promoting the nucleation of  $\beta_1$  phases [31]. Based on the first-principles calculation, the vacancy-binding energy of Zn is calculated to be 0.05 eV, and this positive vacancy-binding energy of Zn might be beneficial to the precipitation of  $\beta_1$  [32].

Based on the previous studies, the formation of basal precipitates in Mg–RE–Zn alloys is likely to be caused by the formation of clusters of RE and Zn atoms [13, 15, 33]. The atomic radius of Mg (0.160 nm) is small than RE (0.182 nm for Nd, 0.180 nm for Gd), but larger than Zn (0.133 nm). Due to the apparent difference in atomic radius, taking the place of an Mg atom with a Gd/Nd atom leads to a compression strain. However, replacing it with a Zn atom results in an extension strain. Therefore, Gd/Nd and Zn atoms are inclined to co-segregate with each other to reduce the matrix elastic strain, contributing to the formation of basal disks [32].

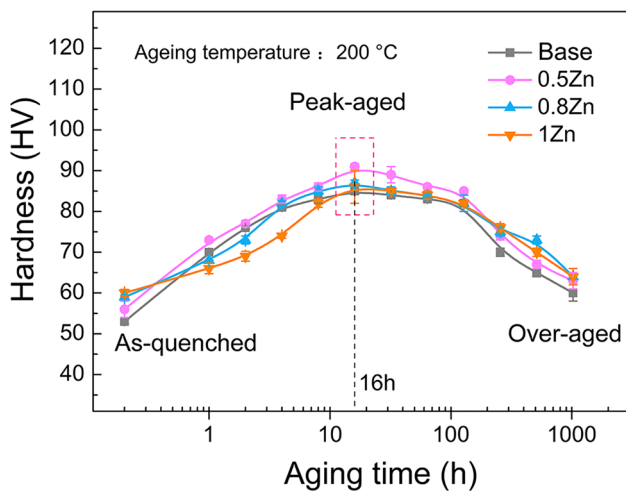


**Fig. 8** Age-hardening characteristics of the base, 0.5Zn, 0.8Zn and 1Zn alloys at 200 °C

### 4.3 Correlation Between the Microstructural Evolution and Mechanical Properties

#### 4.3.1 Enhanced Mechanical Properties of As-Quenched Alloys Associated with Zn Additions

It is noted that the increments in YS of as-quenched alloys associated with 0.5, 0.8 and 1 wt% Zn additions are 2, 12 and 8 MPa, respectively (illustrated in Fig. 14d). Under the as-quenched condition, the strengthening contributions to the YS of alloys are likely to be originated from three aspects: the solute atoms, the grain boundaries and the Zn–Zr phases within the grains of Zn-containing alloys. The additions of Zn primarily affect the YS by influencing these factors.

The contribution of solid solution strengthening can be calculated as [34]:

$$\Delta\sigma_s = B_z A_z^{2/3} \quad (1)$$

where  $B_z$  refers to a constant associated with the element Z, and  $A_z$  represents the atomic fraction of element Z.

As previously reported,  $B_{Zn} = 43 \text{ MPa at}^{-2/3}$ . The solid solution hardening effect of 1 wt% (about 0.37 at.%) Zn atoms is calculated to result in an increase of only 1.02 MPa in yield strength [34]. Namely, the effect of Zn additions on solid solution strengthening can be ignored.

The contribution of grain size to the YS can be expressed by the Hall–Petch equation, as follows [12, 35]:

$$\sigma = \sigma_0 + kd^{-1/2} \quad (2)$$

where  $\sigma_0$  is the friction stress,  $k$  is the Hall–Petch coefficient, and  $d$  is the average grain size.

As indicated in Fig. 4, the average grain sizes of the as-quenched base, 0.5Zn, 0.8Zn and 1Zn alloys are 31, 30, 29 and 27  $\mu\text{m}$ , respectively. By referring to the reported Hall–Petch coefficient of Mg alloy (4.42–39.5  $\text{MPa mm}^{1/2}$ ) [35], the increments of YS by the grain refinements caused by 0.5, 0.8 and 1 wt% Zn additions can be estimated to be about 0.4–3.7, 0.8–7.6 and 1.8–16.0 MPa, respectively. Thus, it can be inferred that the improved YS of as-quenched alloys associated with Zn additions might be mainly ascribed to the grain refinements due to the Zn additions. The Zn–Zr particles in as-quenched Zn-containing alloys do not show an apparent strengthening effect.

Additionally, it is also noticeable that the UTS and EL of as-quenched alloys gradually increase with increasing Zn content. The increments of UTS and EL associated with Zn additions can be attributed to the optimization effect of Zn additions on plasticity. As previously reported, Zn is an effective alloying element for decreasing the stack fault energy (SFE) in Mg alloys [36, 37]. Low SFE is conducive to the formation of stacking faults (SFs) and the activation of non-basal  $\langle c + a \rangle$  slip, thereby effectively improving the plasticity of magnesium alloys at ambient temperature.

#### 4.3.2 Strengthening Effects of Different Precipitate Microstructure

After subjected to the aging treatment, it is noticeable that a large number of precipitates appear within the grains. Table 4 compares the increments of YS ( $\Delta\text{YS} = \text{YS}_{\text{peak-aged}} - \text{YS}_{\text{as-quenched}}$ ) for the peak-aged alloys with different Zn content. The increments of YS mainly come from the formation of precipitates during the aging treatment. It is noticeable that the increment of YS is increased from 45 to 69 MPa with the 0.5 wt% Zn addition. As shown in Table 5, it is noteworthy that the area number density of the prismatic precipitates in the peak-aged 0.5Zn alloys is higher than the peak-aged base alloy. Thus, the higher  $\Delta\text{YS}$  in the 0.5Zn alloy is mainly attributed to the increasing number density of prismatic precipitates. Further increasing the Zn content results in a decrease in the  $\Delta\text{YS}$ . Compared with the 0.5 Zn alloy, the reductions in the  $\Delta\text{YS}$  associated 0.8 and 1 wt% Zn additions are 15 and 11 MPa, respectively. As indicated in Table 5, the high Zn content introduces considerable amounts of basal precipitates. These basal precipitates in Mg–RE–Zn alloys are rich in RE elements [24, 38]. Massive precipitation of basal precipitates will inevitably consume many RE atoms, resulting in the remarkably reduced number density of prismatic precipitates. Thus, the decreases in the  $\Delta\text{YS}$  associated with 0.8 and 1 wt% Zn additions are supposed to be caused by the significantly reduced number density of prismatic precipitates.

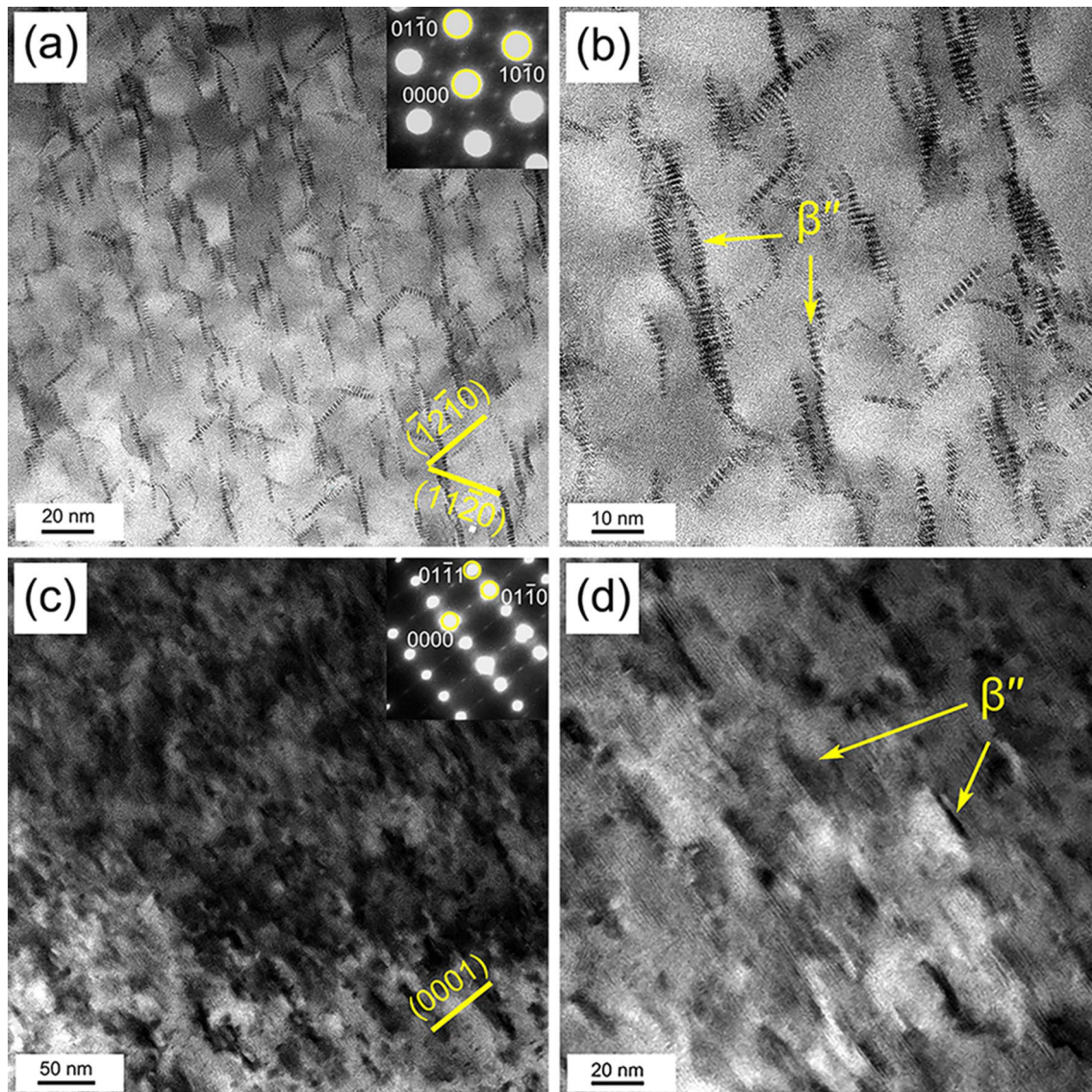


**Fig. 9** BF images showing the morphology and the distribution of  $\beta''$  precipitates in the base alloy subjected to peak-aged treatment. The electron beam is parallel to  $[0001]_{\alpha}$  in **a, b**, and  $[2\ 11\ 0]_{\alpha}$  in **c, d**. The corresponding SAED patterns are inserted in **a, c**

Additionally, as shown in Table 4, the increment of EL ( $\Delta EL = EL_{\text{peak-aged}} - EL_{\text{as-quenched}}$ ) is gradually decreased with increasing Zn content, which indicates that more obvious decreases of plasticity are found in the Zn-containing alloys, especially the 0.8Zn and 1Zn alloys. That is mainly attributed to the promoted precipitation of  $\beta_1$  and basal precipitates associated with Zn additions. Note that the  $\beta_1$  is usually regarded as

a non-shearable precipitate because of the fcc structure incoherent with Mg matrix [38, 39]. At the same time,  $\beta''$  ( $D0_{19}$ ) phases are expected to be shearable to the basal slip as the high degree of interface coherency [39, 40]. Namely, the hindering effect of  $\beta_1$  precipitates to dislocation slip is stronger than  $\beta''$ . Thus, it can be inferred that the precipitation of  $\beta_1$  precipitates decreases the plasticity of alloys more obviously.

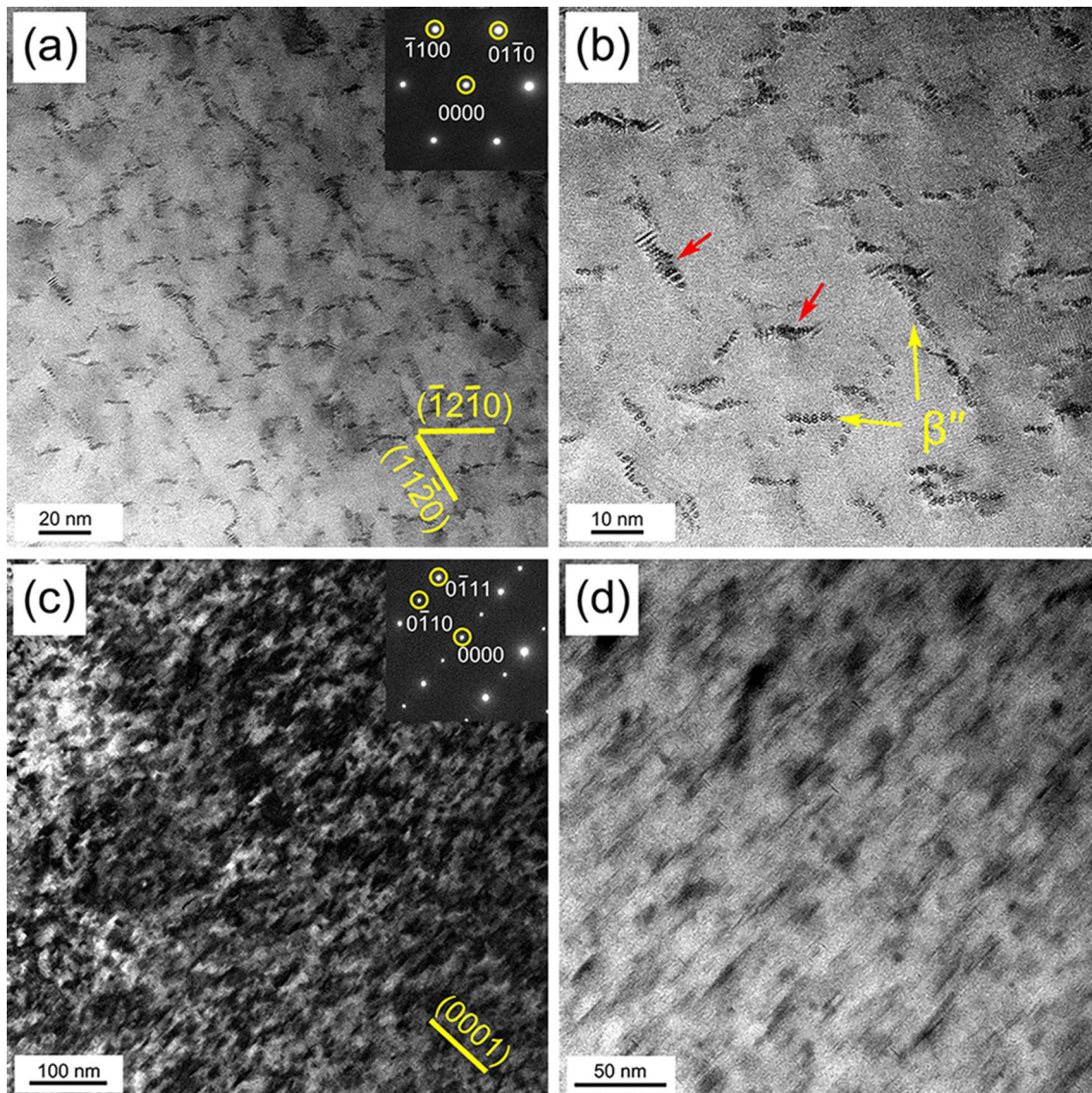


**Fig. 10** TEM micrographs showing precipitate microstructure representative of the peak-aged 0.5Zn alloy: **a, b** BF images recorded parallel to  $[0001]_{\text{Mg}}$  direction; **c, d** BF images recorded parallel to  $[2\ 11\ 0]_{\text{Mg}}$  direction

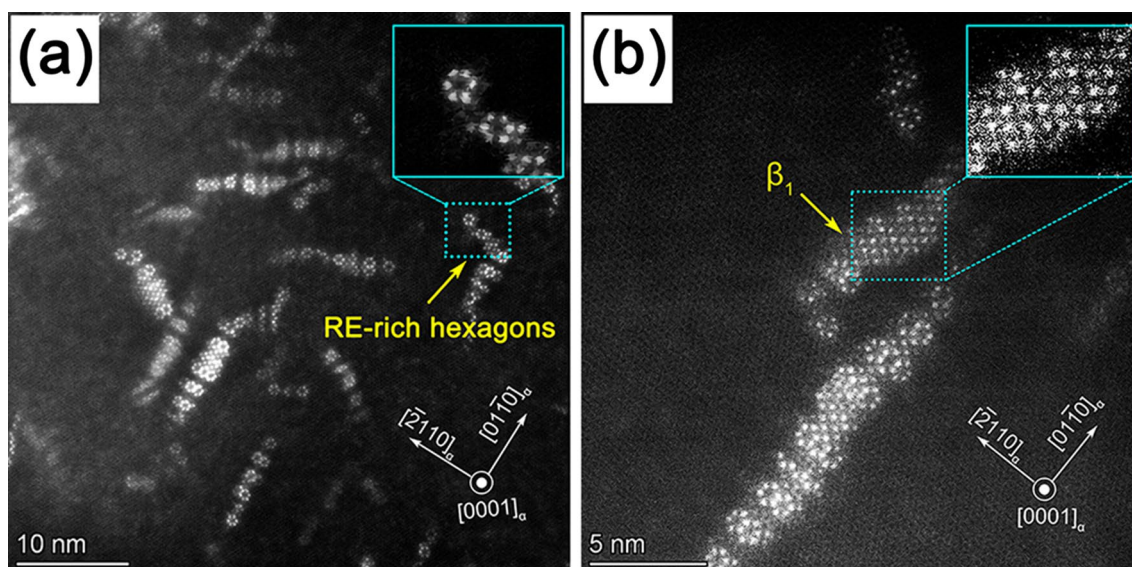


**Fig. 11** HADDF-STEM images showing the precipitates interaction between  $\beta_1$  and  $\beta''$  in the peak-aged 0.5Zn alloy. The magnified region in **a**, **b** shows the identical structure of  $\beta''$  and  $\beta_1$ , respectively. The electron beam is parallel to  $[0001]_{\text{Mg}}$  direction

Moreover, it is noteworthy that  $\beta_1$  precipitates and basal precipitates are Zn-rich precipitates [13, 41]. The precipitation of them is supposed to lower the number of Zn atoms dissolved in Mg matrix. Considering that the solid solution of Zn atoms in the Mg matrix can promote the activation of the non-basal slip system and therefore optimize plasticity [36, 37], it can be inferred that the precipitation of  $\beta_1$  precipitates and basal precipitates is also likely to decrease the plasticity of alloys by consuming the solid Zn atoms in Mg matrix.

## 5 Conclusions

This work investigates the influence of different Zn additions on the microstructure and mechanical properties of cast Mg–3Nd–3Gd–0.5Zr alloy. The following conclusions are obtained:

1. Zn–Zr particles form during solution treatment as a result of Zn addition. As the Zn content increases, the number density of Zn–Zr particles also increases. During the aging treatment, Zn–Zr particles can perform as

the preferential sites for the heterogeneous nucleation of  $\beta_1$ .

2.  $\beta''$  precipitates are the main strengthening precipitates in the peak-aged Zn-free alloy. With 0.5 wt% Zn addition, additional fine prismatic  $\beta_1$  phases form besides  $\beta''$  precipitates. In the peak-aged 0.8Zn alloy,  $\beta_1$  phases are the key strengthening precipitates, accompanied by a scanty distribution of basal precipitates. For the peak-aged 1Zn alloy, the matrix precipitation is characterized by the coexistence of prismatic  $\beta_1$  precipitates and dense basal precipitates.
3. YS and UTS of Mg–3Nd–3Gd– $x$ Zn–0.5Zr alloys undergo the first increase and then decrease variation trend with increasing Zn addition. The peak-aged Mg–3Nd–3Gd–0.5Zn–0.5Zr alloy exhibits the relatively best mechanical properties (YS = 179 MPa, UTS = 301 MPa and EL = 5.3%).

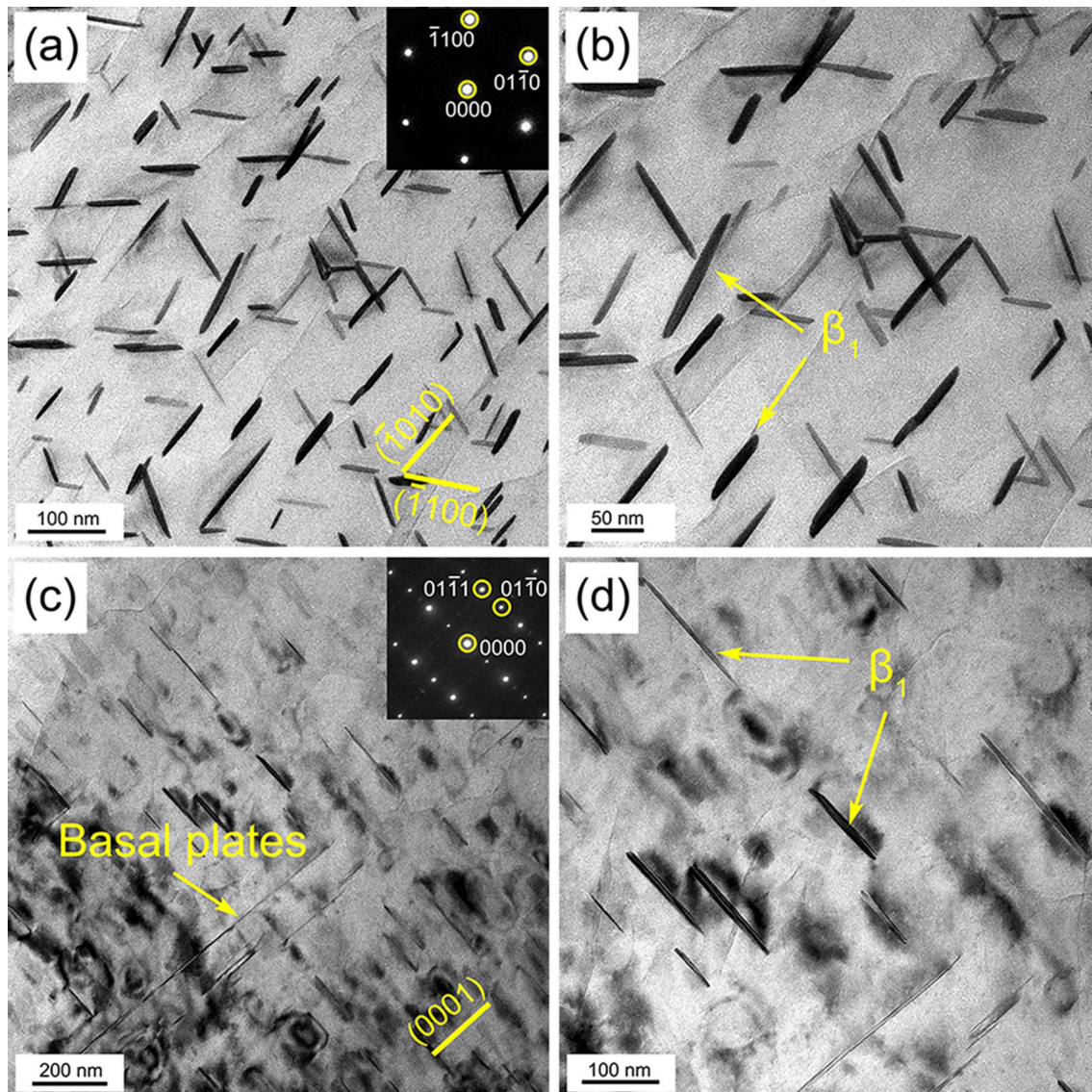


**Fig. 12** BF micrographs showing the precipitates in sample of 0.8Zn alloy peak-aged at 200 °C: **a, b** BF micrographs with the incident beam direction of  $[0001]_{\alpha}$ , demonstrating the distribution of  $\beta_1$  precipitates; **c, d** BF micrographs exhibiting the coexistence of prismatic  $\beta_1$  plates and scanty basal plates ( $\mathbf{B} = [2\ 11\ 0]_{\alpha}$ )

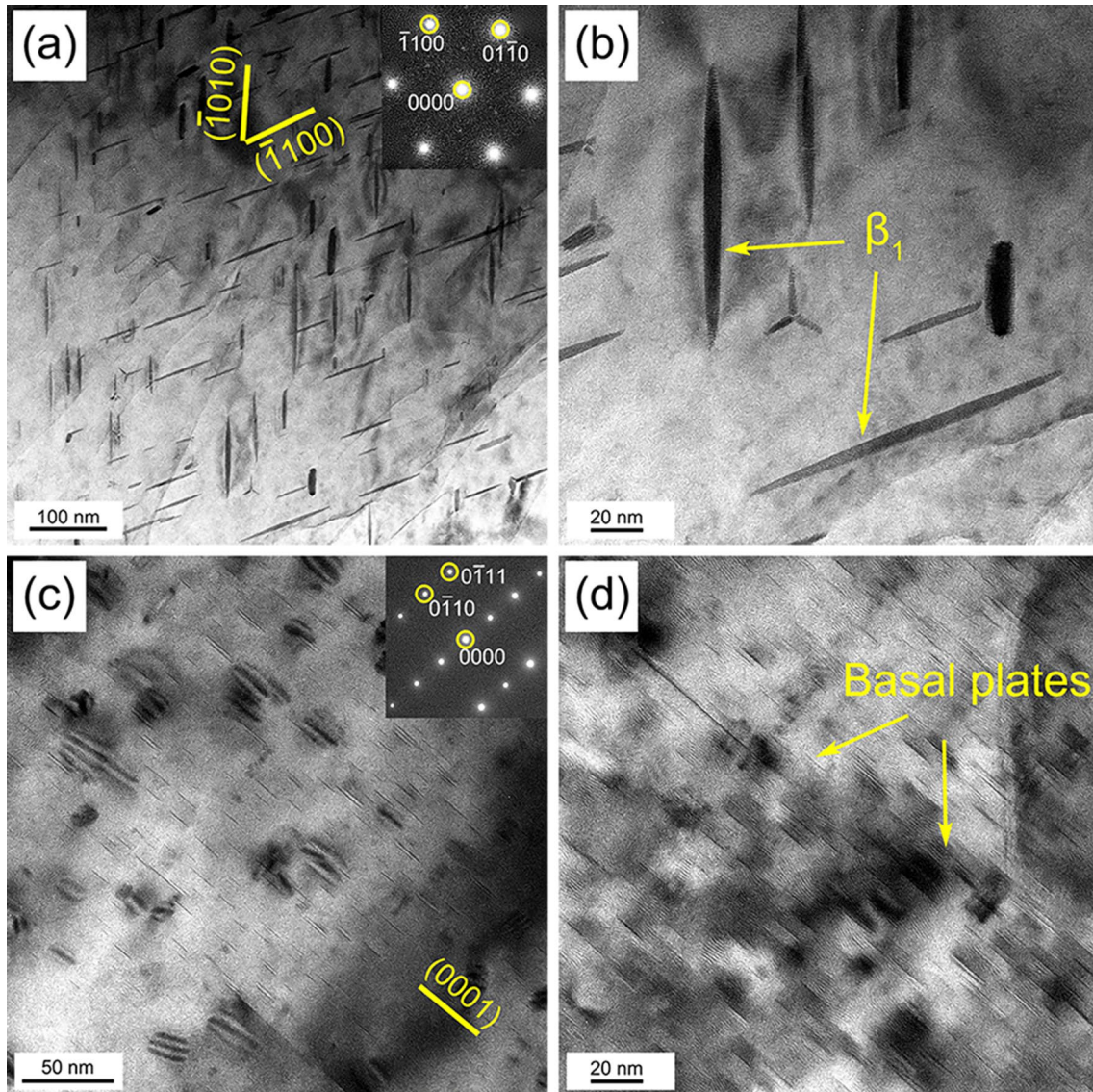


**Fig. 13** BF micrographs showing the precipitate microstructure in sample of the 1Zn alloy peak-aged at 200 °C: **a, b** BF micrographs with the incident beam direction of  $[0001]_{\alpha}$ , demonstrating the distribution of  $\beta_1$  precipitates; **c, d** BF micrographs exhibiting the dense dispersion of basal plates ( $\mathbf{B}=[2\ 11\ 0]_{\alpha}$ )

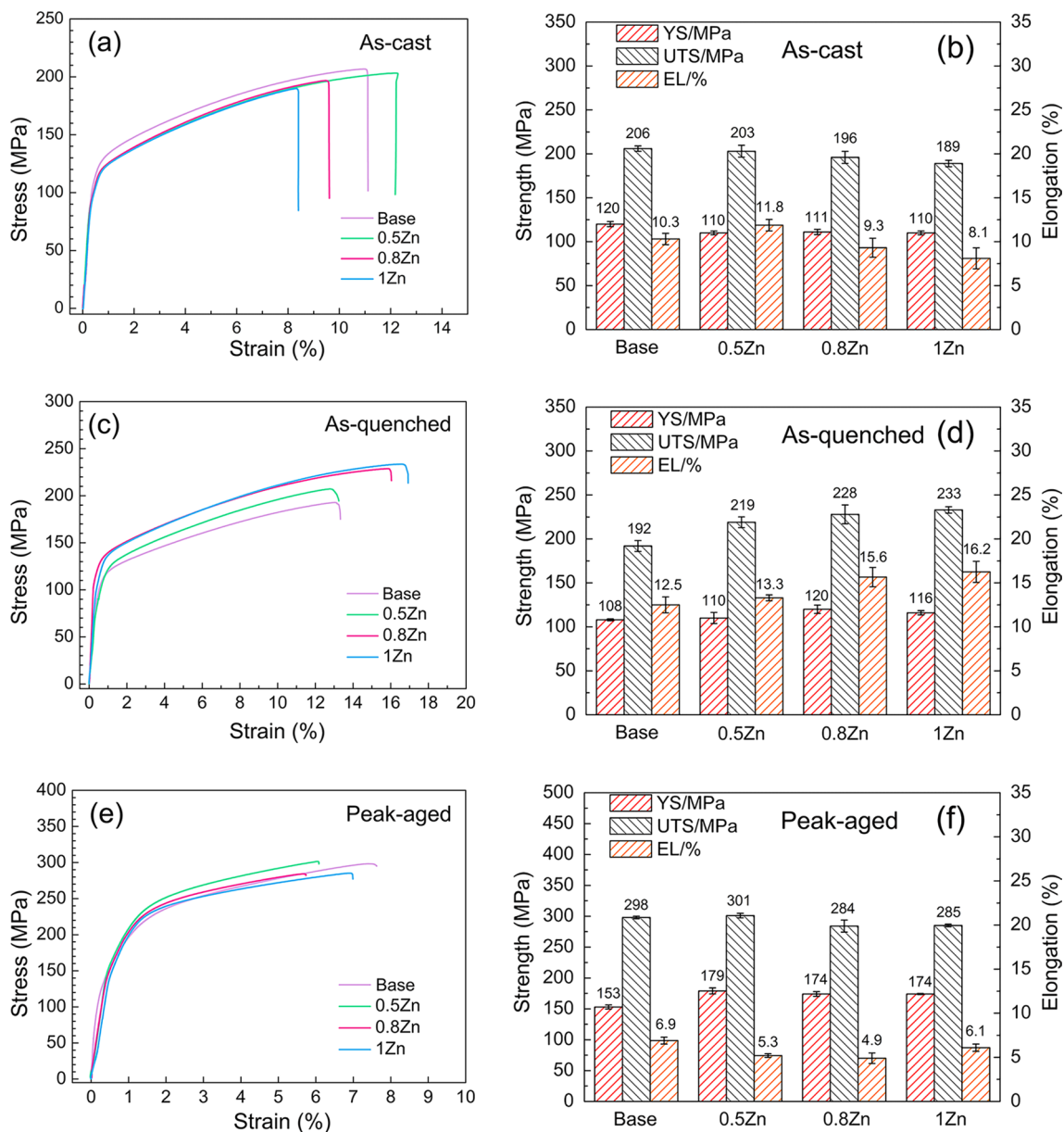


**Fig. 14** Typical engineering strain–stress curves (left column) and mechanical properties (right column) of Mg–3Nd–3Gd–xZn–0.5Zr alloys under different states: **a, b** as-cast; **c, d** as-quenched; **e, f** peak-aged



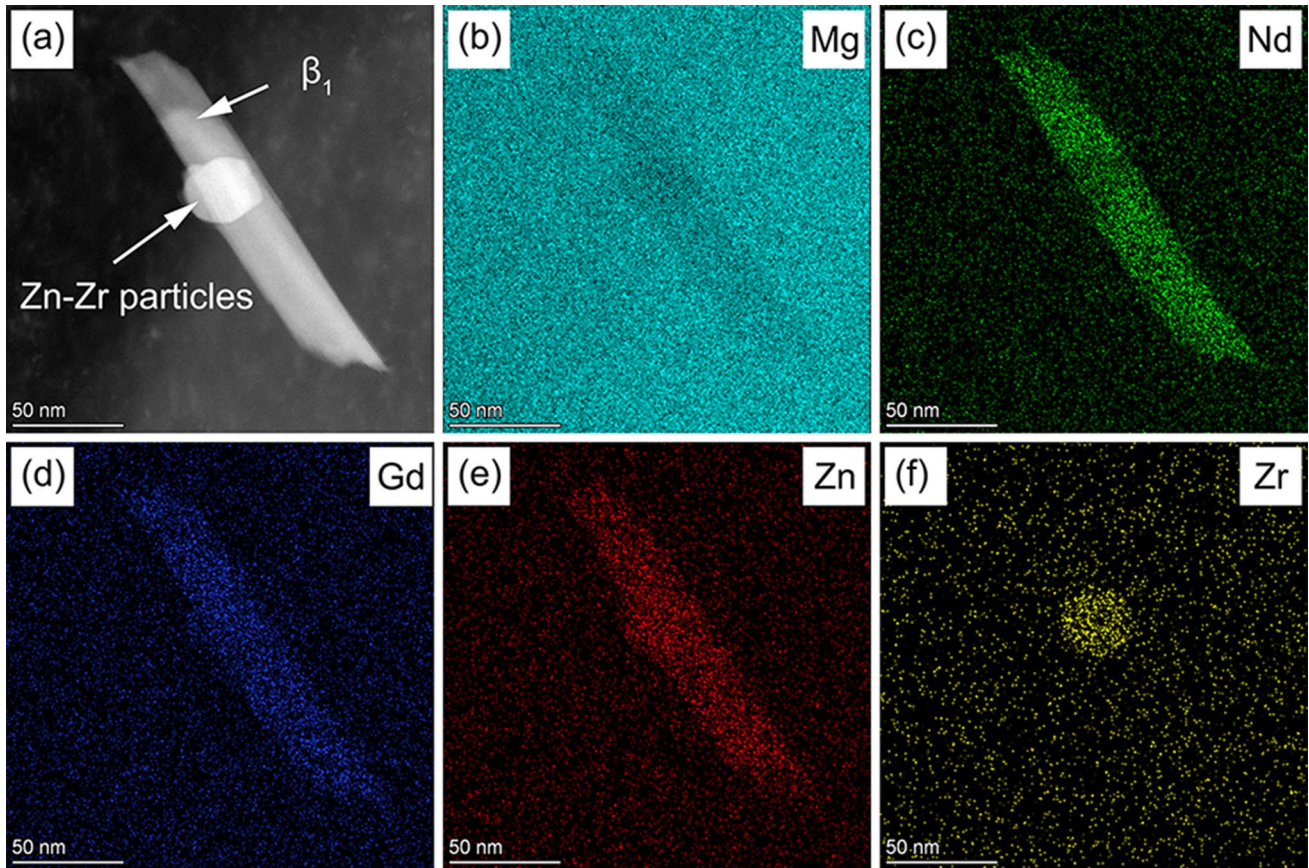


**Fig. 15** **a** HAADF-STEM micrograph of the heat-treated 1Zn alloy (peak-aged at 200 °C for 16 h) illustrating a unique interaction between the globular Zn–Zr particle and  $\beta_1$  precipitate, taken along the  $[0001]_\alpha$  zone axis; elemental maps of **b** Mg; **c** Nd; **d** Gd; **e** Zn, **f** Zr correspond to the **a**

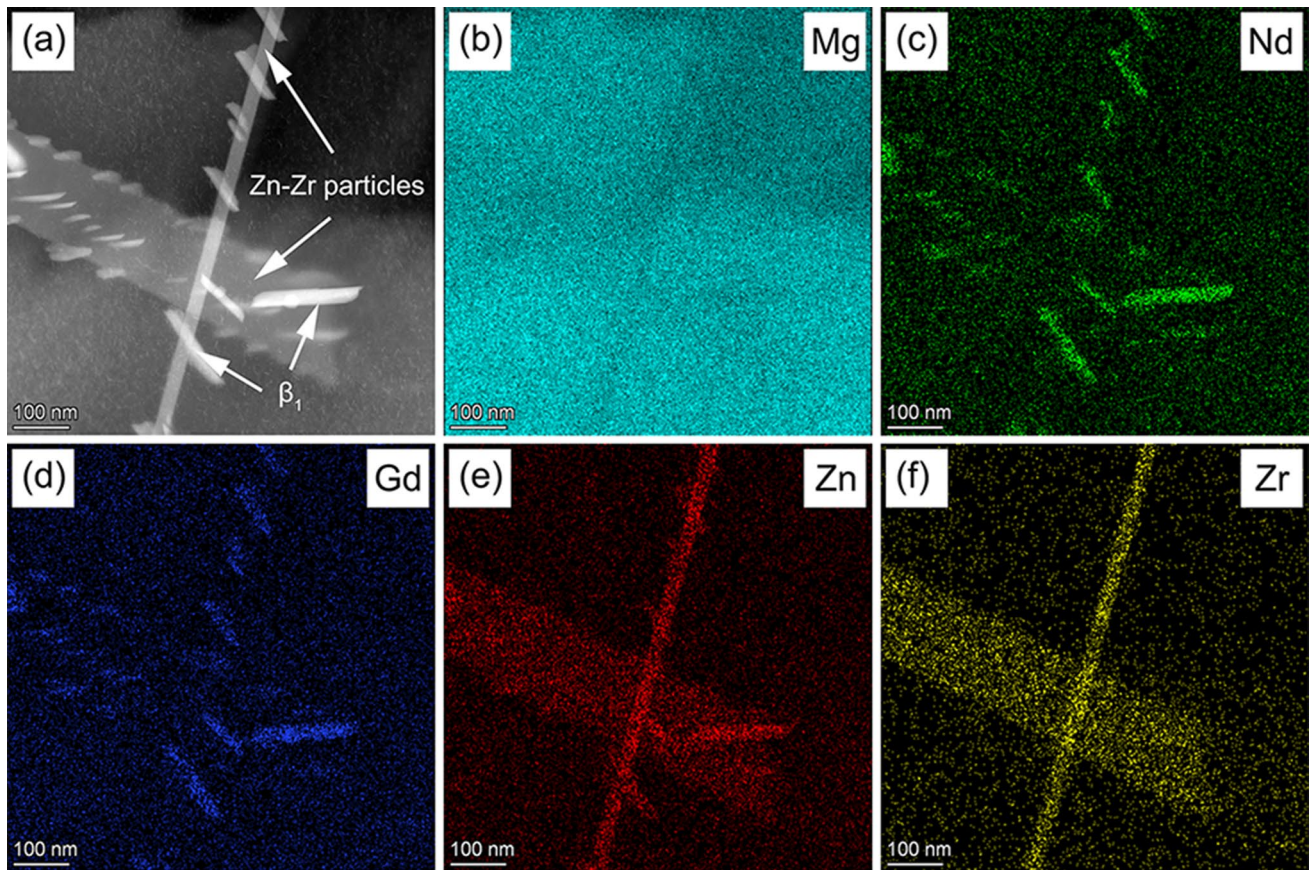


**Fig. 16** a HAADF-STEM micrograph of the heat-treated 1Zn alloy (peak-aged at 200 °C for 16 h) illustrating the unique interaction between rod-like Zn–Zr particles and  $\beta_1$  precipitate, taken along the  $[0001]_a$  zone axis; elemental maps showing the distribution of b Mg; c Nd; d Gd; e Zn, f Zr

**Table 3** Primary precipitates in the peak-aged alloys

Condition	Precipitates after aging at 200 °C			
	Base	0.5Zn	0.8Zn	1Zn
Peak-aged	$\beta''$	$\beta'', \beta_1$	$\beta_1$ , basal plates	$\beta_1$ , basal plates

**Table 4** Comparison of strengthening effects of precipitate microstructures in different peak-aged alloys

Alloys	Base	0.5Zn	0.8Zn	1Zn
$YS_{\text{peak-aged}} - YS_{\text{as-quenched}}$ ( $\Delta YS$ , MPa)	45	69	54	58
$UTS_{\text{peak-aged}} - UTS_{\text{as-quenched}}$ ( $\Delta UTS$ , MPa)	106	82	56	52
$EL_{\text{peak-aged}} - EL_{\text{as-quenched}}$ ( $\Delta EL$ , %)	-5.6	-8.0	-10.7	-10.1

**Table 5** Measured area number density of prismatic precipitates and basal precipitates in peak-aged alloys

	Base alloy	0.5Zn alloy	0.8Zn alloy	1Zn alloy
Area number density of prismatic precipitates ( $m^{-2}$ )	$8.32 \times 10^{15}$	$9.24 \times 10^{15}$	$3.66 \times 10^{14}$	$2.63 \times 10^{14}$
Area number density of basal precipitates ( $m^{-2}$ )	–	–	$1.03 \times 10^{13}$	$2.82 \times 10^{15}$

**Acknowledgements** This research was financially supported by the National Natural Science Foundation of China (Nos. U2037601, 51775334 and 51821001), the National Key Research & Development Program of China (No. 2016YFB0701205), the Joint Innovation Fund of CALT and College (No. CALT2020-TS07), the Open Fund of State Key Laboratory of Advanced Forming Technology and Equipment (No. SKL2020005) and the Research Program of Joint Research Center of Advanced Spaceflight Technologies (No. USCAST2020-14).

## References

- [1] L.L. Rokhlin (ed.), *Magnesium Alloys Containing Rare Earth Metals* (CRC Press, London, 2003)
- [2] L.Y. Jia, W.B. Du, J.L. Fu, Z.H. Wang, K. Liu, S.B. Li, X. Du, *Acta Metall. Sin. Engl. Lett.* **34**, 39 (2020)
- [3] J.L. Li, N. Zhang, X.X. Wang, D. Wu, R.S. Chen, *Acta Metall. Sin. Engl. Lett.* **31**, 189 (2017)
- [4] J. Kubásek, D. Dvorský, J. Veselý, P. Minárik, M. Zemková, D. Vojtěch, *Acta Metall. Sin. Engl. Lett.* **32**, 321 (2018)
- [5] R.G. Li, F. Asghar, J.H. Zhang, G.Y. Fu, Q. Liu, B.T. Guo, Y.M. Yu, S.G. Guo, Y. Su, X.J. Chen, L. Zong, *Acta Metall. Sin. Engl. Lett.* **32**, 245 (2018)
- [6] B. Li, B.G. Teng, D.G. Luo, *Acta Metall. Sin. Engl. Lett.* **31**, 1009 (2018)
- [7] S. DeWitt, E.L.S. Solomon, A.R. Natarajan, V. Araullo-Peters, S. Rudraraju, L.K. Aagesen, B. Puchala, E.A. Marquis, A. van der Ven, K. Thornton, J.E. Allison, *Acta Mater.* **136**, 378 (2017)
- [8] H. Liu, Y.M. Zhu, N.C. Wilson, J.F. Nie, *Acta Mater.* **133**, 408 (2017)
- [9] E.L.S. Solomon, V. Araullo-Peters, J.E. Allison, E.A. Marquis, *Scr. Mater.* **128**, 14 (2017)
- [10] W.H. Wang, D. Wu, R.S. Chen, X.N. Zhang, *J. Mater. Sci. Technol.* **34**, 1236 (2018)
- [11] X. Xia, A. Sanaty-Zadeh, C. Zhang, A.A. Luo, D.S. Stone, *Calphad* **60**, 58 (2018)
- [12] H. Xie, G. Wu, X. Zhang, W. Liu, W. Ding, *Mater. Charact.* **175**, 111076 (2021)
- [13] T. Honma, T. Ohkubo, S. Kamado, K. Hono, *Acta Mater.* **55**, 4137 (2007)
- [14] Y.Q. Chi, C. Xu, X.G. Qiao, M.Y. Zheng, *J. Alloys Compd.* **789**, 416 (2019)
- [15] J.F. Nie, K. Oh-ishi, X. Gao, K. Hono, *Acta Mater.* **56**, 6061 (2008)
- [16] W. Rong, Y. Wu, Y. Zhang, M. Sun, J. Chen, L. Peng, W. Ding, *Mater. Charact.* **126**, 1 (2017)
- [17] K. Hagihara, A. Kinoshita, Y. Sugino, M. Yamasaki, Y. Kawamura, H.Y. Yasuda, Y. Umakoshi, *Acta Mater.* **58**, 6282 (2010)
- [18] G. Garcés, G. Requena, D. Tolnai, P. Pérez, P. Adeva, A. Stark, N. Schell, *J. Mater. Sci.* **49**, 2714 (2014)
- [19] L.S. Wang, J.H. Jiang, B. Saleh, Q.Y. Xie, Q. Xu, H. Liu, A.B. Ma, *Acta Metall. Sin. Engl. Lett.* **33**, 1180 (2020)
- [20] Y. Xu, D. Xu, X. Shao, E.H. Han, *Acta Metall. Sin. Engl. Lett.* **26**, 217 (2013)
- [21] Y. Zhou, P. Fu, L. Peng, D. Wang, Y. Wang, B. Hu, M. Liu, A.K. Sachdev, W. Ding, *J. Magnes. Alloy* **7**, 113 (2019)
- [22] G. Jia, E. Guo, L. Wang, Y. Feng, Y. Chen, *Results Phys.* **11**, 152 (2018)
- [23] X. Gao, B.C. Muddle, J.F. Nie, *Philos. Mag. Lett.* **89**, 33 (2009)
- [24] J.F. Nie, *Metall. Mater. Trans. A* **43**, 3891 (2012)
- [25] J. Tan, Y. Dong, H.X. Zhang, Y.H. Sun, B.Z. Sun, Y. Qi, *Scr. Mater.* **172**, 130 (2019)
- [26] Y. Zhang, W. Rong, Y. Wu, L. Peng, J.F. Nie, N. Birbilis, *J. Alloys Compd.* **777**, 531 (2019)
- [27] D. Zhang, Q. Yang, B. Li, K. Guan, N. Wang, B. Jiang, C. Sun, D. Zhang, X. Li, Z. Cao, J. Meng, *J. Alloys Compd.* **805**, 811 (2019)
- [28] W.Z. Wang, D. Wu, R.S. Chen, Y. Qi, H.Q. Ye, Z.Q. Yang, *J. Alloys Compd.* **832**, 155 (2020)
- [29] H.M. Zhu, G. Sha, J.W. Liu, H.W. Liu, C.L. Wu, C.P. Luo, Z.W. Liu, R.K. Zheng, S.P. Ringer, *Nanoscale Res. Lett.* **7**, 300 (2012)
- [30] H. Xie, G. Wu, X. Zhang, J. Zhang, W. Ding, *Mater. Sci. Eng. A* **817**, 141292 (2021)
- [31] J.F. Nie, B.C. Muddle, *Acta Mater.* **48**, 1691 (2000)
- [32] D. Wang, P. Fu, L. Peng, Y. Wang, W. Ding, *Mater. Charact.* **153**, 157 (2019)
- [33] X. Gao, J.F. Nie, *Scr. Mater.* **58**, 619 (2008)
- [34] I. Toda-Caraballo, E.I. Galindo-Nava, P.E.J. Rivera-Díaz-del-Castillo, *Acta Mater.* **75**, 287 (2014)
- [35] Z.M. Li, A.A. Luo, Q.G. Wang, L.M. Peng, P.H. Fu, G.H. Wu, *Mater. Sci. Eng. A* **564**, 450 (2013)
- [36] D. Zhang, D. Zhang, F. Bu, X. Li, B. Li, T. Yan, K. Guan, Q. Yang, X. Liu, J. Meng, *J. Alloys Compd.* **728**, 404 (2017)
- [37] H.S. Jang, B.J. Lee, *Scr. Mater.* **160**, 39 (2019)
- [38] D.H. Ping, K. Hono, J.F. Nie, *Scr. Mater.* **48**, 1017 (2003)
- [39] E.L.S. Solomon, E.A. Marquis, *Mater. Lett.* **216**, 67 (2018)
- [40] Z. Huang, C. Yang, L. Qi, J.E. Allison, A. Misra, *Mater. Sci. Eng. A* **742**, 278 (2019)
- [41] J.F. Nie, X. Gao, S.M. Zhu, *Scr. Mater.* **53**, 1049 (2005)